

1 Nixon, C. W., Bull, J. M. and Sanderson, D. J. (2014). Localized vs distributed  
2 deformation associated with the linkage history of an active normal fault,  
3 Whakatane Graben, New Zealand. *Journal of Structural Geology*, 69, (A), 266-  
4 280. ([doi:10.1016/j.jsg.2014.06.005](https://doi.org/10.1016/j.jsg.2014.06.005)).

5

6 **Localized vs distributed deformation associated with**  
7 **the linkage history of an active normal fault, Whakatane**  
8 **Graben, New Zealand**

9 **Casey W. Nixon<sup>1\*</sup>, Jonathan M. Bull<sup>1</sup>, David J. Sanderson<sup>123</sup>**

10 <sup>1</sup> Ocean and Earth Science, University of Southampton, National  
11 Oceanography Centre Southampton, SO14 3ZH, UK.

12 <sup>2</sup> Faculty of Engineering and the Environment, University of Southampton,  
13 SO17 1BJ, UK.

14 <sup>3</sup> BP Exploration Operating Company Limited. Chertsey Road, Sunbury-on-  
15 Thames, TW16 7BP, UK.

16 \* Corresponding Author – [c.w.nixon@noc.soton.ac.uk](mailto:c.w.nixon@noc.soton.ac.uk)

17 **Keywords:** *Fault network; Distributed faulting; Localized faulting; Strain*  
18 *localization; Spatial heterogeneity; Normal faults; fault linkage*

19 **Abstract**

20 The deformation associated with an active normal fault is investigated at a high  
21 temporal resolution (c. 10<sup>4</sup> yr). The Rangitaiki Fault (Whakatane Graben, New  
22 Zealand) and its adjacent faults accommodated an overall extension of ~0.83%  
23 oriented at ~N324°E over the past 17 kyr. This is consistent along strike, but

24 the pattern of faulting that accommodates this strain defines two different spatial  
25 domains. To the SW, one domain is characterized by a few large faults, with  
26 >80% of strain localized onto geometrically and kinematically linked segments  
27 of the main fault. This produces marked heterogeneity in the spatial distribution  
28 of strain across the graben. In contrast, to the NE, a domain of distributed  
29 faulting is characterized by numerous small faults contributing to the overall  
30 deformation, with only ~35% of strain localized onto the Rangitaiki Fault. The  
31 transition from distributed to localized deformation is attributed to an increase in  
32 linkage maturity of the Rangitaiki Fault. Progressive strain localization has  
33 been ongoing within the network over the last 17 kyr, with localization of fault  
34 activity increasing by ~12%, indicating this process occurs over kyr time periods  
35 that only reflect a few earthquake events.

36

37

## 38 **1. Introduction**

39 Fault networks often contain a few large faults that accumulate much greater  
40 displacement than the surrounding faults. These large faults dominate the  
41 system and accommodate the majority of the strain (e.g. Walsh et al., 2003;  
42 Putz-Perrier and Sanderson, 2010). They often grow by the interaction of fault  
43 segments that eventually link (Cartwright et al., 1995; Childs et al., 1996;  
44 Peacock, 2002) developing a range of structures (i.e. relay zones; Long and  
45 Imber, 2011) and damage (i.e. tip damage; Kim et al., 2003). Hence, a fault  
46 network will evolve from a more distributed population of faults that become  
47 better connected with time to form a system dominated by a few larger faults  
48 (e.g. Cowie et al., 1995; Nicol et al., 1997; Meyer et al., 2002; Gawthorpe et al.,

49 2003; Walsh et al., 2003; Cowie et al., 2005; Soliva and Schultz, 2008).  
50 Understanding the organization of deformation around such large faults is  
51 important for understanding fault network growth and development but also for  
52 seismic hazard analysis by providing insights into the distribution of  
53 displacement between interacting faults and during fault ruptures. Therefore,  
54 the aim of this paper is a high-resolution investigation of the spatial and  
55 temporal accumulation of strain within a fault network containing a large  
56 through-going fault whose growth by segment is known.

57 To better understand the organization of faulting we also investigate the  
58 distribution of strain within the related fault network in terms of spatial  
59 heterogeneity (e.g. Putz-Perrier and Sanderson 2008a). In general, when strain  
60 is uniformly distributed across a network of evenly spaced faults the strain  
61 distribution can be described as 'homogenous'. However, if some faults  
62 accommodate more strain than others and the faults are not evenly spaced then  
63 the distribution of strain can be termed 'heterogeneous'. The distribution of  
64 strain accommodated by a network of faults in the upper crust has been studied  
65 spatially, across a range of scales (e.g. Bailey et al., 2005; Putz-Perrier and  
66 Sanderson, 2008a; Nixon et al., 2012). These have added to our understanding  
67 of strain localization (e.g. Meyer et al., 2002; Walsh et al., 2003; Taylor et al.,  
68 2004; Bailey et al., 2005; Soliva and Schultz, 2008) and the contribution of  
69 smaller faults to overall total strains (e.g. Walsh et al., 1991; Marrett and  
70 Almendinger, 1992; Putz-Perrier and Sanderson 2008b, 2010). Although there  
71 has been much work investigating how strain is distributed onto different size  
72 structures within a fault population (e.g. Marrett and Almendinger, 1991, 1992;  
73 Walsh and Waterson, 1992; Pickering et al., 1996), only a few studies have

74 directly measured this together with the spatial heterogeneity in strain  
75 distribution (i.e. Putz-Perrier and Sanderson, 2008a).

76 In this study we investigate a normal fault network associated with the active  
77 Rangitaiki Fault, which is a large displacement fault within the Whakatane  
78 Graben, New Zealand (Figure 1). This currently active fault network displaces  
79 an area which has good stratigraphic resolution, a sedimentary sequence  
80 containing identifiable horizons of known age, where the sedimentation rate is  
81 similar to the dip-slip rate on the faults, and where it is possible to correlate from  
82 hanging-wall to foot-wall. (Lamarche et al., 2000; Taylor, 2004; Bull et al.,  
83 2006). Thus, a high-resolution seismic dataset that images small faults with  
84 throws down to ~1 m provides a high-fidelity record of normal fault activity over  
85 the past 17 kyr. Therefore, this fault network can be investigated and analysed  
86 at a much higher spatial and temporal resolution than achieved in previous  
87 studies, which have been limited by the resolution of their seismic data (e.g.  
88 Walsh et al., 2003). Hence, we aim to use the Rangitaiki Fault and the  
89 surrounding fault network to:

- 90 1. Characterize the organization of faulting and accumulation of  
91 displacement within the active fault network, investigating the  
92 variations along strike of the Rangitaiki Fault;
- 93 2. Examine the displacement distribution and fault activity within the  
94 fault network at a very high temporal resolution (e.g. 1-10 kyr time  
95 scales);
- 96 3. Measure the strain accommodated by the fault system;

- 97           4. Investigate any spatial heterogeneity in the distribution of extensional  
98           strain and how this relates to variations in fault numbers and sizes;  
99           5. Better understand heterogeneity within a fault network, particularly  
100          with respect to the linkage history of major faults.

101

## 102   **2. Geological background**

### 103   ***2.1. Tectonic setting***

104   The study area is in the most active part of the Whakatane Graben, which is  
105   located in the Bay of Plenty, New Zealand (Figure 1). The graben is an active  
106   part of the Taupo Volcanic Zone (TVZ) – a zone of Quaternary back-arc rifting  
107   and volcanism associated with the oblique westward subduction of the Pacific  
108   plate beneath the Australian plate at the Hikurangi Margin. The Whakatane  
109   Graben lies beneath the Rangitaiki Plain and the northern part of the graben  
110   extends onto the continental shelf (Figure 1) (Nairn and Beanland, 1989;  
111   Wright, 1990; Bull et al., 2006). The graben itself is bound by the White Island  
112   Fault to the SE and the Rurima Ridge to the NW. The White Island Fault forms  
113   a prominent fault scarp that separates the dip-slip dominated graben from the  
114   North Island Dextral Shear Belt, whereas the Rurima Ridge is a topographic  
115   high separating the Whakatane Graben to the SE from the Motiti Graben to the  
116   NW (Bull et al., 2006; Lamarche et al., 2006).

117   An extensive seismic reflection survey of the Motiti and Whakatane Grabens  
118   (Lamarche et al., 2000) includes regional seismic profiles as well as a detailed  
119   seismic study over the Rangitaiki Fault within the Whakatane Graben. Seismic  
120   reflection data and multibeam bathymetry indicate that the Whakatane Graben

121 is dominated by large NW-dipping active normal faults, that displace the top 3  
122 km of sediment including sediments deposited in the last 17 kyr (Lamarche et  
123 al., 2000; Taylor, 2004). The faults are spaced at 1-3 km and produce large  
124 fault-bound blocks that are cut by smaller synthetic and antithetic faults  
125 (Lamarche et al., 2006). Analysis of faulting and subsidence of the post-glacial  
126 transgressive surface, dated at 17 ka, indicates that the Whakatane Graben has  
127 an average subsidence rate of 2 mm/yr (Wright, 1990) and extends horizontally  
128 at a rate of 2.9 +/- 0.7 mm/yr (Lamarche et al., 2006). Within the onshore  
129 continuation of the rift are numerous active faults, for example the 1987 March  
130  $M_L$  6.3 earthquake on the Edgecumbe fault (Nairn and Beanland, 1989), that  
131 offset geomorphic structures on the Rangitaiki Plains and indicate a late  
132 Holocene (<2 kyr) subsidence rate of ~3 mm/yr (Begg and Mouslopoulou,  
133 2010), consistent with those determined for the offshore Whakatane Graben  
134 (Wright, 1990).

## 135 ***2.2. Linkage and activity of the Rangitaiki Fault***

136 The Rangitaiki Fault and its subsidiary faults (Figure 2) have very little or no  
137 surface expression in the present day sea bed surface (Figure 2b) as they are  
138 part of a fully filled system (Bull et al., 2006; Lamarche et al., 2006). This has  
139 allowed its strain history to be fully determined from the seismic reflection data  
140 (e.g. Taylor et al., 2004; Bull et al., 2006). Unlike the Rangitaiki Fault, the  
141 history of the White Island Fault is difficult to unravel due to an incomplete  
142 footwall stratigraphy.

143 In general, the Rangitaiki Fault is the most active structural element of the  
144 Whakatane Graben (Taylor et al., 2004; Bull et al., 2006; Lamarche et al.,  
145 2006). It is a typical normal fault with dip values  $>59^\circ$  in the top 2 km of

146 sediment (Figure 2b; Taylor, 2003) and has growth strata in its hanging wall  
147 (Figure 2b and c). Taylor et al. (2004) calculate the displacement accumulation  
148 on the Rangitaiki Fault for the three horizons imaged in the multi-channel  
149 seismic data (Figure 2b; MCS1 – 3; age  $300 \pm 100$  ka,  $770 \pm 290$  ka, and  $1340$   
150  $\pm 510$  ka) as well as the post-glacial transgressive surface in the high-resolution  
151 seismic data (Figure 2c; H4; age  $17 \pm 1$  ka). See Taylor et al., 2004 for full  
152 description of data and stratigraphic framework. Overall the Rangitaiki Fault  
153 has accumulated up to 830 m of dip-slip motion since  $\sim 1.3$  Ma (Figure 2b;  
154 Taylor et al., 2004). During this period the Rangitaiki Fault has been shown to  
155 have grown by the linkage of five fault segments (R1-R5; Figures 2 and 3).  
156 Taylor et al. (2004) demonstrate that each segment initially grew by tip  
157 propagation in the early stages of growth, with low displacement rates of  $0.72$   
158  $\pm 0.23$  mm/yr (Figure 3a and b). The fault system became fully linked between  
159 300 ka and 17 ka with marked increases in displacement rate up to a maximum  
160 of  $3.4 \pm 0.2$  mm/yr (Figure 3c and d; Taylor et al., 2004). Of particular note is  
161 the breaching of the relay ramp between R1 and R3 by the transfer fault R2  
162 (Figure 3c).

163 Using high-resolution seismic data (Figure 2c), Bull et al. (2006) investigated  
164 the post-linkage accumulation of displacement on the segments (R1-R5) of the  
165 Rangitaiki Fault since 17 ka. In general, displacement rate patterns were highly  
166 irregular over smaller time intervals (2-3 kyr), with larger fault segments  
167 sometimes producing values of zero displacement for some time intervals,  
168 whereas longer time intervals of at least 9 kyr produced more regular  
169 displacement rate patterns (Figure 3d; Bull et al., 2006) similar to those for time  
170 periods of 300 kyr (Figures 2a and 3c; Taylor et al., 2004). They also

171 investigated the linkage maturity of the Rangitaiki Fault by identifying which fault  
172 segments are geometrically linked and, potentially, kinematically linked (i.e. a  
173 coherent displacement profile between geometrically linked segments).

174 Bull et al., (2006) only analyse the post-linkage displacement accumulation on  
175 the segments of the Rangitaiki Fault. However, large faults rarely form without  
176 associated deformation, hence, we further develop this by investigating the  
177 post-linkage accumulation of displacement for the fault network adjacent to the  
178 Rangitaiki Fault. Furthermore, we determine the partitioning of strain between  
179 the Rangitaiki Fault and its related fault network in order to characterise their  
180 kinematic relationship and behaviour.

181

## 182 **3. Methodology**

### 183 **3.1. Seismic data and interpretation**

184 The high-resolution seismic reflection data comprises 46 boomer profiles that  
185 were taken across the main Rangitaiki Fault, as summarized in Bull et al.  
186 (2006). The boomer profiles were spaced between 100-200 m covering an area  
187 of approximately 7.5 x 7.5 km (Figure 1), imaging the last 17 +/- 1 kyr of  
188 sedimentation across the central part of the Rangitaiki Fault, providing  
189 information on the top ~60 m of stratigraphy with a vertical resolution of ~0.5 m.

190 The seismic profiles were interpreted using a 3-D seismic interpretation  
191 software to pick faults and horizons. Faults were correlated across profiles  
192 using geographic positioning of each fault pick and studying throw gradients  
193 along faults (e.g. Freeman et al., 2010). This involved identifying isolated faults  
194 and interacting faults (i.e. splays) by realistic patterns of throw along their

195 profiles. Four strongly reflective horizons (H1-H4) were identified (Figure 4).  
196 These are laterally continuous and well correlated across each boomer profile;  
197 these were used to constrain the evolution of the fault network during the last 17  
198 +/- 1 kyr. The ages of each horizon are given in Table 1, and are discussed in  
199 more detail by Bull et al. (2006).

### 200 **3.2. Throw measurements and analysis**

201 Where horizons are cut by a fault, they are projected towards the fault plane to  
202 correct for localized deformation processes, such as fault drag, around the fault  
203 planes (Mansfield and Cartwright, 1996; Bull et al., 2006). The vertical  
204 component of dip separation (throw) at each fault was calculated for all four  
205 horizons from manual picks of the hanging wall and footwall cut-offs of each  
206 horizon. We used an average interval velocity of  $1550 \text{ ms}^{-1}$  for the  
207 uncompacted near surface sediments, which was constrained by geophysical  
208 logging of 43 piston cores (Taylor et al., 2004). As the faults are normal in  
209 nature, have very steep dips ( $>70^\circ$ ) and affect flat lying sediments, the throw  
210 approximates the fault displacement. For information on relative errors of throw  
211 measurements and horizon ages see Bull et al. (2006).

212 The measured throws are used to analyse the deformation across the fault  
213 network by calculating throw rates and strain values for each horizon and  
214 different areas of the fault network. Throw rates are calculated for each fault at  
215 different time periods using the throws for different horizons (Table 1). 2-D  
216 strain was analysed by calculating the heave for all the faults using fault dips  
217 derived by Taylor (2003) from multichannel seismic reflection data. The  
218 average dips for the fault network are  $61^\circ$  for the Rangitaiki Fault,  $65^\circ$  for the

219 hanging wall faults and 68° for the footwall faults. The total extension of all the  
 220 faults on each boomer profile was then calculated from their cumulative heave.  
 221 3-D strain values were determined using the methodology proposed in Peacock  
 222 and Sanderson (1993), which uses the fault orientation and dip separation to  
 223 construct a Lagrangian strain tensor (Figure 5). This involves calculating the  
 224 eigenvalues and eigenvectors of the Lagrangian strain tensor ( $E_{ij}$ ) when  
 225 sampling faults from a plane:

$$226 \quad E_{ij} = \frac{1}{A} \times \sum \left( t \times \frac{D_{ij} + D_{ji}}{2} \right) \quad (1)$$

227 where  $A$  is the sample area,  $t$  is the fault trace-length and  $D_{ij}$  is the displacement  
 228 tensor (Figure 5). Fault interactions within a normal fault network can often  
 229 produce complex 3-D strains, however, as we do not have slip orientation data  
 230 for these normal faults we assume a dip-slip displacement for these faults  
 231 (Figure 5). As these are normal faults sampled on a plane we apply a weighting  
 232 factor ( $w = 1/\sin(\text{fault dip})$ ) to the displacement tensor (Peacock and Sanderson  
 233 1993), which corrects for the orientation bias between the sample plane and the  
 234 fault dip, hence:

$$235 \quad D_{ij} = ws \begin{pmatrix} n_1 u_1 & n_1 u_2 & n_1 u_3 \\ n_2 u_1 & n_2 u_2 & n_2 u_3 \\ n_3 u_1 & n_3 u_2 & n_3 u_3 \end{pmatrix} \quad (2)$$

236 Where  $s$  is the displacement and unit vectors  $n$  and  $u$  are normal to the fault  
 237 plane and parallel to the slip direction, respectively (Figure 5). Thus, where a  
 238 fault dips  $\theta$  towards  $\Phi$  (Figure 5), then:

$$239 \quad \mathbf{n} = ( -\cos\Phi \sin\theta, -\sin\Phi \sin\theta, \cos\theta ) \quad \text{and} \quad \mathbf{u} = ( \cos\Phi \cos\theta, \sin\Phi \cos\theta, \sin\theta )$$

240 The 3-D strain has a minimum, intermediate and maximum extension axis  
241 producing a plunge and azimuth for each axis. For a more detailed  
242 methodology on the strain calculation see Peacock and Sanderson (1993).

243 The throw rates and strain values are used to analyse the spatial and temporal  
244 variation in deformation across the fault network. We use fault maps weighted  
245 by throw rate as well as along strike profiles of strain and cumulative throw, for  
246 different time intervals.

247

## 248 **4. Variations in faulting and throw**

### 249 **4.1. Geometry and organization of faulting**

250 The fault network associated with the Rangitaiki Fault is illustrated in Figure 6.  
251 We divide the faults into three groups: the Rangitaiki Fault, its hanging wall  
252 faults and its footwall faults. The Rangitaiki Fault consists of a number of fault  
253 segments that link and form its main trace-length as defined by Bull et al. (2006)  
254 (R1-R5; Figure 6a). The hanging wall and footwall faults are the faults that form  
255 in the hanging wall fault block to the NW and footwall fault block to the SE of the  
256 Rangitaiki Fault, respectively (Figure 6a).

257 Rose diagrams of the fault trends indicate that each fault group is dominated by  
258 approximately ENE-trending faults (Figure 6b). The Rangitaiki Fault and the  
259 footwall (FW) faults trend  $\sim$ N058°E and  $\sim$ N059°E, respectively, whereas the  
260 hanging wall (HW) faults show a slightly oblique fault trend of  $\sim$ N071°E. These  
261 orientations are consistent with the general fault trends throughout the  
262 Whakatane Graben (e.g. Lamarche et al., 2006). In general, the fault network  
263 is dominated by N-dipping normal faults with the longest and largest being the

264 Rangitaiki Fault. This dominance is also reflected in HW fault group but not in  
265 the FW fault group, which has almost equal proportions of both N-dipping and  
266 S-dipping faults (Figure 6b).

267 The number of faults within the fault network increases along strike towards the  
268 NE from 8 faults at profile 104 (Figure 4a) to 26 faults at profile 137 (Figure 4c).  
269 This is due to increased numbers of faults in the HW and FW blocks, which we  
270 will investigate further by comparing the distribution of throw within the SW and  
271 NE regions (defined by Location 1 in Figure 6a).

#### 272 **4.2. Spatial distribution and accumulation of throw**

273 Although the number of faults increases from SW to NE (Figure 6), the  
274 cumulative throws at H4 for each profile are very similar, with values of 120 m,  
275 111 m and 116 m for profiles 104, 124 and 137, respectively. This indicates  
276 that the throw is localized onto fewer faults for profile 104 and becomes  
277 distributed across more faults for profiles 124 and 137. Furthermore, the throw  
278 map in Figure 7d illustrates that to the SW of Location 1 throw appears to be  
279 mainly localized onto the Rangitaiki Fault, whereas to the NE of Location 1 the  
280 throw is distributed throughout the hanging wall and footwall blocks with less  
281 throw occurring on the Rangitaiki Fault.

282 Figure 7 also shows an accumulation of throw through time for the entire fault  
283 network (Figure 7a) as well as showing the contribution of the Rangitaiki Fault  
284 and its HW and FW faults (Figure 7b and 7c). We group the HW and FW faults  
285 together as they approximately contribute even amounts deformation. The  
286 cumulative throw profiles (Figure 7) are broadly similar in shape for each  
287 horizon. Furthermore, the total cumulative throw profile (Figure 7a) reflects the

288 smooth profile of the Rangitaiki Fault (Figure 7b) up until Location 1 (i.e. 0-2800  
289 m strike distance), but NE of Location 1 (i.e. 2800-6500 m strike distance) the  
290 total cumulative throw profile (Figure 7a) is similar to the profile of the HW and  
291 FW faults (Figure 7c).

292 For H4 (17 ka) the Rangitaiki Fault steadily decreases in throw from ~90 m to  
293 ~20 m from SW-NE (Figure 7b), which is consistent with results from Bull et al.  
294 (2006). In contrast, the cumulative throw contributed by the HW and FW faults  
295 (Figure 7c) abruptly increases to the NE of Location 1. SW of location 1 the  
296 throw profile is smooth with low throws of ~20 m at H4, however, the throw  
297 profile then increases abruptly in steps at Locations 1, 2, 3, 4 and 5 (Figure 7c).  
298 These jumps in throw are attributed to the introduction of different fault  
299 segments in the HW and FW blocks as indicated by numbered circles in Figure  
300 7d.

### 301 **4.3. Fault activity**

302 Average throw rates for the entire fault network are shown in Table 2 for  
303 different time intervals over the last 17 kyr. The average throw rate of the  
304 network ranges from a maximum of 11.1 mm/yr between 17 ka – 13.9 ka to a  
305 minimum of 4.9 mm/yr between 13.9 ka – 11.4 ka. This is true for all parts of  
306 the network with the throw rates of the Rangitaiki Fault and the HW and FW  
307 faults both producing maximum and minimum values for the same time  
308 intervals. The average throw rates and the throw rate maps in Figure 8 clearly  
309 show that between 17 ka -13.9 ka the fault network was most active, including  
310 the Rangitaiki Fault as well as the HW faults and FW faults. However, the throw  
311 rates for all the other time intervals appear to have been relatively constant with  
312 an overall average throw rate of 6.7 mm/yr over the last 17 kyr (Table 2).

313 The contribution of the HW and FW faults to the total throw rate of the fault  
314 network is consistently greater than the contribution of the Rangitaiki Fault for  
315 all time intervals (Table 2). However, the proportion of the total average throw  
316 rate contributed by the Rangitaiki Fault does increase from 36.0% to 48.4%  
317 through time. This suggests that the activity of the fault network has been  
318 steadily localizing onto the Rangitaiki Fault and that the HW and FW faults have  
319 become proportionally less active over the last 17 kyr. This can also be seen in  
320 the throw rate maps, which show fairly consistent activity for the Rangitaiki Fault  
321 but steadily decreasing throw rates on many of the individual HW and FW faults  
322 with time, in particular the FW faults of the network (Figure 8).

323 The total throw rate profile of the entire fault network is consistent along strike,  
324 particularly for the longer time intervals (i.e. 17 ka - present and 9 ka - present;  
325 Figures 9a and 9e). In general, the Rangitaiki Fault throw rate decreases from  
326 SW to NE for each time interval (Figure 9). However, the HW and FW faults  
327 throw rate profile is more variable especially for shorter time intervals (i.e.  
328 Figure 9b and 9c). Where there is localized faulting to the SW of Location 1, all  
329 the throw rate profiles are relatively smooth and show a constant throw rate.  
330 However, at the transition from localized faulting to distributed faulting, Location  
331 1, there is a marked jump in the throw rate within the HW and FW faults (Figure  
332 9). This is seen across all of the time intervals and indicates that the transition  
333 is abrupt and persistent.

334

## 335 **5. Distribution of extensional strain**

336 Faults that form a fault network will accommodate an overall strain, but this may  
337 not be distributed evenly throughout a fault network. Some domains may

338 accommodate greater strains than others (e.g. Nixon et al., 2011) and some  
339 individual faults may contribute more strain than others (e.g. Putz-Perrier and  
340 Sanderson, 2008a, 2008b). In this section we investigate the spatial distribution  
341 of extensional strain and examine the partitioning of strain between different  
342 faults within the fault network.

### 343 **5.1. Strain partitioning of HW and FW faults vs Rangitaiki Fault**

344 The 3-D strain for H4 has been calculated for the entire study area as well as  
345 the localized domain and distributed domain, using the fault trace-lengths and  
346 their dip azimuths. The maximum extension of the entire fault network is 0.83%  
347 plunging at  $\sim 13^\circ$  towards N324°E (Table 3) with negligible extension in the  
348 intermediate axis of deformation. Furthermore, the proportion of strain  
349 contributed by the Rangitaiki Fault is approximately equal to the strain  
350 accommodated by the HW and FW faults (Table 3).

351 The values of maximum extension for the domains of localized and distributed  
352 faulting are also similar with maximum extensions of 0.83% and 0.85%,  
353 respectively, indicating that there is an overall strain compatibility along the  
354 strike of the fault network. Although the overall extension values are consistent,  
355 the ratio of strain contributed by the Rangitaiki Fault and the HW and FW faults  
356 varies between the domains (Table 3). The HW and FW faults contribute  $\sim 65\%$   
357 of the extension in the distributed domain but only  $\sim 15\%$  of the extension in the  
358 localized domain. Furthermore, the orientation of maximum extension differs  
359 slightly between the two areas with a maximum extension orientation of  
360  $15^\circ/\text{N}315^\circ\text{E}$  for the localized domain and  $12^\circ/\text{N}327^\circ\text{E}$  for the distributed domain.  
361 These orientations are controlled by the Rangitaiki Fault in the localized domain  
362 and the HW and FW faults in the distributed domain (Table 3), indicating that

363 the overall strain of a fault network is not always accommodated by the large  
364 fault and can vary locally along strike of the fault system.

365 An overall 2-D strain for the fault network can be calculated by summing the  
366 total fault extension of the each boomer line and then dividing by the total  
367 number of lines. At H4, the fault network accommodates an overall extension of  
368 0.78% orientated approximately NW-SE, which is consistent with values  
369 calculated in the 3-D strain analysis. The overall percentage extensions of each  
370 boomer line are plotted in an along strike strain profile in Figure 10a. This also  
371 shows the strain profiles of the Rangitaiki Fault (black) and the HW and FW  
372 faults (grey). The strain profiles are similar to the cumulative throw profiles  
373 (Figure 3), showing a steady decrease in strain for the Rangitaiki Fault and  
374 abrupt step-like increases in strain accommodated by the HW and FW faults.  
375 At location 1 the overall strain profile across the fault network reaches a  
376 minimum, which marks the transition from localized faulting to distributed  
377 faulting (Figure 10a).

378 Figure 10b shows the contribution to strain by each individual fault along  
379 boomer lines 104, 124 and 137 to show the along strike variability in the strain  
380 distribution. Line 104 goes through the area of localized faulting and has very  
381 few faults which accommodate the strain. In general, two fault segments of the  
382 Rangitaiki Fault accommodate ~86% of the overall strain for line 104 (Figure  
383 10b). Therefore, the majority of strain is localized onto the Rangitaiki Fault  
384 within the domain of localized faulting.

385 Lines 124 and 137 are within the domain of distributed faulting and have many  
386 more faults than line 104 (Figures 4 and 6). The Rangitaiki Fault does not  
387 accommodate as much of the overall strain in the domain of distributed faulting

388 as it does within the domain of localized faulting, accommodating only 56% and  
389 33% of the overall extension for boomer lines 124 and 137, respectively (Figure  
390 10b). This shows a progressive increase in strain accommodated by the HW  
391 and FW faults within the area of distributed faulting as the strain transfers from  
392 the Rangitaiki Fault onto the surrounding structures. It also indicates that the  
393 degree of strain localization onto the Rangitaiki Fault decreases along strike of  
394 the fault network from SW-NE. This is important as it shows that the largest  
395 faults do not necessarily dominate the deformation throughout the entire fault  
396 network.

## 397 **5.2. Spatial heterogeneity of extensional strain and faulting**

398 Quantifying the spatial heterogeneity of extensional strain and faulting  
399 throughout the fault network allows us to assess the individual contributions of  
400 each fault to the overall strain. In general, we compare the cumulative  
401 distributions of faulting and extensional strain against a uniform distribution (i.e.  
402 a straight line distribution on Figure 11a). Putz-Perrier and Sanderson (2008a)  
403 show that the extent to which the observed data distribution departs from the  
404 uniform distribution can be used as a measure of heterogeneity. They calculate  
405 a simple non-parametric quantity  $V = |D^+| + |D^-|$ , where  $D^+$  and  $D^-$  represent the  
406 maximum deviation above and below the cumulative uniform distribution,  
407 respectively (e.g. Figure 11). This is then normalized by dividing by the  
408 cumulative total in order to compare data from different line samples. Hence,  
409 for fault frequency  $V_f = (|D_f^+| + |D_f^-|) / n$  and for strain  $V_s = (|D_s^+| + |D_s^-|) / E$ ,  
410 where  $n$  = number of faults and  $E$  = total extension. Values of  $V_f$  and  $V_s$  vary  
411 from 0 to 1, with heterogeneity increasing towards 1. For a more detailed  
412 description of the methodology see Putz-Perrier and Sanderson (2008a).

413 Normalized cumulative distributions of fault frequency and extensional strain for  
414 lines 104, 124 and 137 are shown as examples in Figure 11. These show that  
415 the spatial heterogeneity of both faulting and extensional strain varies along  
416 strike of the fault network with line 137 conforming more to a uniform distribution  
417 than line 104. This is supported by the values for  $V_f$  and  $V_s$  which both  
418 decrease from line 104 to line 137 (Figure 11a, b and c). We further investigate  
419 the along strike variation by applying this technique to all boomer lines and the  
420 results are shown in Table 4 and Figure 11d and e. The results show a  
421 significant difference in heterogeneity between the domains of distributed and  
422 localized faulting which changes abruptly at location 1 in Figure 11. In general,  
423 within the domain of distributed faulting there is some heterogeneity for fault  
424 frequency ( $V_f < 0.4$ ) and extensional strain ( $V_s < 0.6$ ), whereas the domain of  
425 localized faulting has a much higher heterogeneity ( $V_f > 0.4$ ;  $V_s > 0.6$ ). This  
426 difference between the two domains is further emphasized by the cross-plot of  
427  $V_f$  and  $V_s$  in Figure 12a. The data show a strong correlation between the  
428 distribution of faulting and the heterogeneity of extensional strain (Figure 12a),  
429 consistent with data presented by Putz-Perrier and Sanderson (2008b).

430 There is no correlation between the total fault extension on each boomer line  
431 and variations in  $V_f$  and  $V_s$  (Figure 12b), indicating that the heterogeneity within  
432 the network is independent of bulk-extension. This is in agreement with other  
433 studies that cover a greater range of bulk-extensions (i.e. Moriya et al., 2005;  
434 Putz-Perrier and Sanderson, 2008b). However, there is a correlation between  
435 both heterogeneity measures and the proportion of strain localized onto the  
436 Rangitaiki Fault (Figure 12c and d). This shows that an increase in the amount  
437 of strain localized onto the Rangitaiki Fault results in a proportional increase in

438 the spatial heterogeneity of extensional strain (Figure 12c). Furthermore, the  
439 heterogeneity in fault distribution is independent of strain localization when only  
440 20-60% of strain is localized onto the Rangitaiki Fault but increases when >60%  
441 of strain is localized onto the Rangitaiki Fault (Figure 12d).

442

## 443 **6. Discussion**

### 444 **6.1. Localized vs distributed faulting**

445 The results indicate that the amount of deformation is similar throughout the  
446 Rangitaiki Fault network with overall values of cumulative throw, throw rate and  
447 strain remaining relatively constant along strike of the network over the last 17  
448 kyr (Figures 6a, 7a and 8; Table 3). However, the amount of deformation  
449 accommodated by the different parts of the fault network varies. We observe  
450 two clear domains within the fault network that behave differently – a domain of  
451 localized faulting and a domain of distributed faulting.

452 The domain of localized faulting (e.g. Figure 13a) is characterized by a few  
453 individual large faults accommodating the majority of the strain (i.e. >80% of the  
454 strain is localized onto the Rangitaiki Fault; Table 3). The overall deformation  
455 localized onto the Rangitaiki Fault produces much heterogeneity in the spatial  
456 distribution of extensional strain and faulting within the domain (i.e.  $V_f > 0.4$  and  
457  $V_s > 0.6$ ; Figures 11 and 12). In contrast, the domain of distributed faulting  
458 (e.g. Figure 13b) is characterized by numerous small faults contributing to the  
459 overall deformation, with only ~35% of the strain localized onto the Rangitaiki  
460 Fault (Table 3). An increased number of faults with less deformation localized  
461 onto the Rangitaiki Fault results in less heterogeneity within the domain of

462 distributed faulting (i.e.  $V_f < 0.4$  and  $V_s < 0.6$ ; Figures 11 and 12). The  
463 variations in  $V_s$  and  $V_f$  indicate that spatial heterogeneity within the fault  
464 network increases when more strain is localized onto a single fault. Therefore,  
465 fault networks with localized deformation are significantly more heterogeneous,  
466 i.e. faults are not evenly spaced and the extensional strain contribution of each  
467 individual fault is highly variable, than networks where deformation is more  
468 distributed.

469 The presence of both localized and distributed regimes of faulting within a fault  
470 system has also been observed by Soliva and Schultz (2008) who describe  
471 areas of distributed faulting, within the basalt plains of the Main Ethiopian Rift,  
472 giving way to localized border faults. Furthermore, Soliva and Schultz (2008)  
473 review statistical analyses of large fault populations identifying the size-  
474 distributions, throw-length relationships, overlap, spacing and linkage of faults  
475 that characterize the localized and distributed end-member regimes of faulting.  
476 This has shown that fault populations within localized regimes produce self-  
477 similar relationships with interdependent parameters, whereas within distributed  
478 regimes these relationships are scale-dependant (i.e. Soliva and Schultz, 2008).  
479 In order to investigate these relationships a large number of faults that span  
480 different scales are needed, which is not always possible. Our methodologies  
481 allow the characterization of distributed and localized domains, without such a  
482 large population of faults, by analysis of the differences in the spatial distribution  
483 of strain and faulting (Figure 13).

484 The transition from the localized domain to the distributed domain shows a  
485 steady decrease in the proportion of strain localized onto the main Rangitaiki  
486 Fault (Figure 10). The transition within the HW and FW faults occurs more

487 abruptly with a jump in throw rate and strain at the boundary between the two  
488 domains (i.e. location 1). Within the domain of distributed faulting the throw  
489 contributed by the HW and FW faults further increases in a series of steps  
490 (Figures 7c and 9a), which occur as more faults are introduced to the network to  
491 accommodate the decrease in throw on the Rangitaiki Fault (Figure 7d).  
492 Although there appears to be a spatially abrupt transition between the domains  
493 in terms of HW and FW faults, the gradual introduction of more faults to the fault  
494 network within the domain of distributed faulting indicates interaction between  
495 the faults within the two domains. Nixon et al. (2011) show similar interactions  
496 between domains within a strike-slip fault network in north Devon (U.K.), where  
497 a change in fault polarity produce variations in the strain profile across the fault  
498 network. They show lows in the strain profile in zones accommodating the  
499 transition between the two domains of faulting, which is similar to the strain  
500 profile across the Rangitaiki Fault network where a low in the strain profile is  
501 seen at the transition between the area of localized faulting and distributed  
502 faulting (Figure 10a). Nixon et al. (2011) make the point that although there is a  
503 change in the overall maximum extension of these accommodation zones, they  
504 still maintain a strain compatibility between the interacting domains. -We argue  
505 that this is probably the case for the Rangitaiki Fault system as fault segment  
506 R2 (Figures 3 and 6) has an oblique orientation to the general extension  
507 direction so may have an additional oblique component to its slip vector.

## 508 **6.2. Temporal patterns of fault activity**

509 The domains of localized faulting and distributed faulting are observed at  
510 different time intervals over the last 17 kyr including intervals as small as 2-3  
511 kyr. These time intervals only reflect a few earthquake events on each

512 individual fault (Bull et al., 2006) and it is known that throw rates and  
513 accumulation on individual faults are highly variable over small time intervals  
514 (i.e. Bull et al., 2006; Mouslopoulou et al., 2009). This explains the slight  
515 variations in overall throw rate for the different time intervals (Table 2).  
516 However, the distribution of these events over many faults throughout the entire  
517 fault network preserves the overall pattern of throw distribution across the  
518 network for all time intervals (i.e. Figures 7 and 9). This agrees with Nicol et al.  
519 (2010), who show that variability in displacement rate decreases with an  
520 increase in fault numbers, indicating that the pattern of faulting and  
521 displacement rate is more ordered for a population of faults than for an  
522 individual fault.

523 As the time intervals in this study reflect only small numbers of earthquakes it is  
524 possible that many of the faults in the HW and FW blocks may have ruptured  
525 simultaneously during a large magnitude event on the Rangitaiki Fault. Such a  
526 rupture pattern is characteristic of the region as revealed by the numerous faults  
527 that ruptured on the Rangitaiki Plains during the 1987 March,  $M_L$  6.3  
528 Edgecumbe earthquake (Nairn and Beanland, 1989).

### 529 **6.3. Linkage and localization**

530 The changes in the distribution of faulting and proportion of strain localized onto  
531 the Rangitaiki Fault, between the two domains, can be attributed to the linkage  
532 history of the main fault. Taylor et al. (2004), on the basis of multichannel  
533 seismic reflection data, showed that the major segments of the Rangitaiki fault  
534 became linked at depth some time after 300 kyr, and before 17 kyr (e.g. Figure  
535 3c). Furthermore, Bull et al. (2006) looked at the segment interactions of the  
536 Rangitaiki Fault derived from near-surface sediments over the last 17 kyr by

537 comparing the displacement profiles of each fault segment (R1-R5; Figure 3d).  
538 This analysis identified whether segments were geometrically linked and/or  
539 kinematically linked by displacement transfer between segments (e.g. Figure  
540 3d).

541 We note that segments of the Rangitaiki Fault that were linked geometrically but  
542 only partially linked kinematically (Bull et al., 2006) are within the domain of  
543 distributed faulting, suggesting linkage is not well established (e.g. Figure 3d).  
544 In contrast, the segments that were geometrically linked and kinematically  
545 linked (Bull et al., 2006) are within the domain of localized faulting, indicating  
546 linkage was more established within this domain (e.g. Figure 3d). Hence, the  
547 change in domain is related to the maturity and linkage evolution of the  
548 Rangitaiki Fault. Therefore, as fault linkage becomes more established, the  
549 deformation within the network evolves from a distributed pattern to being more  
550 localized on the main fault.

#### 551 **6.4. Progressive strain localization**

552 As the amount of strain localized onto the Rangitaiki Fault changes between the  
553 two domains, we argue that the pattern of faulting and throw distribution is  
554 caused by progressive strain localization as the segment linkage of the  
555 structure becomes more established. Although this study only covers the last  
556 17 kyr, and this interval is short in relation to the history of the Rangitaiki Fault  
557 network, there is evidence, summarized in Table 2, that this localization has  
558 increased by ~12% over this timespan.

559 Progressive strain localization has been recognised and described as an  
560 important process in the development of fault populations. For example, Walsh  
561 et al. (2003) identify strain localization onto large individual faults within a

562 growth fault population during a 16 Myr phase of rifting in the inner Moray Firth,  
563 northern North Sea. Furthermore, Cowie et al. (2005) observe a regional  
564 localization of strain over a 40 Myr period in the Viking Graben, North Sea. This  
565 is characterized by the systematic migration of fault activity towards the rift axis  
566 and is shown to be related to the thermal evolution of the lithosphere by  
567 mechanical models of lithospheric extension (Cowie et al., 2005). The  
568 localization of strain within the Rangitaiki Fault network is an example of  
569 particular importance as it shows that these processes are still occurring after  
570 initial linkage of the main fault system. Furthermore, this study has shown that  
571 this process can happen gradually by the transfer of fault activity from  
572 surrounding structures onto the main Rangitaiki Fault without the abrupt death  
573 of smaller faults (i.e. Table 2; Figure 8). It also illustrates that progressive strain  
574 localization not only occurs over Myr time scales of but also over kyr time  
575 scales. Therefore, progressive strain localization occurs over a range of length  
576 and time scales, thus affecting the overall architecture of rifts as well as the  
577 organization of faulting around individual large faults.

578

## 579 **7. Conclusions**

580 We have investigated the organization of minor faulting, the accumulation of  
581 throw and the distribution of strain around the Rangitaiki Fault in the Whakatane  
582 Graben, NZ. We used high-resolution seismic reflection imagery of the last ~  
583 17 kyr of sedimentation to derive a high quality fault population associated with  
584 this larger fault. We observe a consistent pattern of faulting and distribution of  
585 throw within the fault network across numerous time intervals over the last 17  
586 kyr, indicating a kinematic coherency with time.

587 In general, the fault network changes in character along strike and can be  
588 separated into two domains, which have different characteristics and different  
589 patterns of faulting but preserve the strain compatibility between the two  
590 domains. We describe these domains as an area of localized faulting to the SW  
591 and an area of distributed faulting to the NE, and explain the two domains in  
592 terms of the linkage history of different parts of the Rangitaiki Fault. The area of  
593 localized faulting has:

- 594 a) Very few faults in the hanging wall and footwall blocks of the Rangitaiki  
595 Fault.
- 596 b) The majority of the strain (>80%) localized onto the main Rangitaiki  
597 Fault, which controls the orientation of maximum extension within the  
598 domain.
- 599 c) Smooth throw and strain profiles which are similar to the main Rangitaiki  
600 Fault.
- 601 d) Much heterogeneity in the spatial distribution of both faulting ( $V_f > 0.4$ )  
602 and extensional strain ( $V_s > 0.6$ ).

603 In contrast, the area of distributed faulting has:

- 604 a) Many faults in the hanging wall and footwall blocks of the Rangitaiki Fault  
605 that contribute to the overall deformation.
- 606 b) The majority of the strain (>65%) accommodated by the numerous  
607 hanging wall and footwall faults with only ~35% localized onto the  
608 Rangitaiki Fault. The hanging wall and footwall faults also influence the  
609 orientation of maximum extension.

610 c) Throw and strain profiles influenced by the hanging wall and footwall  
611 faults creating increasing step-like increments as more faults are  
612 introduced to the network.

613 d) Weak heterogeneity in the spatial distribution of faulting ( $V_f < 0.4$ ) and  
614 extensional strain ( $V_s < 0.6$ ).

615 The transition between the domains is marked by a steady change in throw on  
616 the Rangitaiki Fault but with an abrupt jump in throws of the hanging wall and  
617 footwall faults. Overall the two domains are interacting with each other and  
618 illustrate the influence that a large fault can have on the organization of faulting  
619 and distribution of deformation of the surrounding fault network.

620 The change in character of the fault network reflects the process of progressive  
621 strain localization onto the Rangitaiki Fault and is influenced by the evolution of  
622 linkage along strike of the fault. Our results indicate that this process is still  
623 ongoing as activity has continued to localize onto the Rangitaiki Fault over the  
624 last 17 kyr. We show that the distribution of faulting and extensional strain  
625 within the fault network becomes significantly more heterogeneous when more  
626 strain is localized to a single large structure within the fault population.

627 Ultimately, the interacting fault population surrounding a large fault changes as  
628 the system evolves with deformation becoming more localized and spatial  
629 heterogeneity increasing.

630

## 631 **8. Acknowledgements**

632 Nixon was supported by a NERC CASE studentship (NE/H524922/1) with BP.

633 The seismic reflection profiles illustrated in this paper were collected in

634 collaboration with Geoffroy Lamarche and Phil Barnes of NIWA. This work was  
635 funded by the Natural Environment Research Council (GR3/11862) and the  
636 New Zealand Foundation for Research Science and Technology (contract  
637 CO1X0203). We thank reviewers Conrad Childs and Chris Jackson for their  
638 insightful and constructive reviews which helped to improve the paper.

639

## 640 **9. References**

- 641 Bailey, W.R., Walsh, J.J., Manzocchi, T., 2005. Fault populations, strain distribution  
642 and basement fault reactivation in the East Pennines Coalfield, UK. *Journal of*  
643 *Structural Geology* 27, 913-928.
- 644 Begg, J.G., Mouslopoulou, V., 2010. Analysis of late Holocene faulting within an active  
645 rift using lidar, Taupo Rift, New Zealand. *Journal of Volcanology and Geothermal*  
646 *Research* 190, 152-167.
- 647 Bull, J.M., Barnes, P.M., Lamarche, G., Sanderson, D.J., Cowie, P. A., Taylor, S.K.,  
648 Dix, J.K., 2006. High-resolution record of displacement accumulation on an active  
649 normal fault: implications for models of slip accumulation during repeated  
650 earthquakes. *Journal of Structural Geology* 28, 1146–1166.
- 651 Cartwright, J.A., Trudgill, B., Mansfield, C.S., 1995. Fault growth by segment linkage:  
652 an explanation for scatter in maximum displacement and trace length data from  
653 the Canyonlands Grabens of SE Utah. *Journal of Structural Geology* 17, 1319–  
654 1326.
- 655 Childs, C., Nicol, A., Walsh, J.J., Watterson, J., 1996. Growth of vertically segmented  
656 normal faults. *Journal of Structural Geology* 18, 1389–1397.
- 657 Cowie, P.A., Sornette, D., Vanneste, C., 1995. Multifractal scaling properties of a  
658 growing fault population. *Geophysical Journal International* 122, 457-469.

659 Cowie, P.A., Underhill, J.R., Behn, M., Lin, J., Gill, C., 2005. Spatio-temporal evolution  
660 of strain accumulation derived from multi-scale observations of Late Jurassic  
661 rifting in the northern North Sea: A critical test of models for lithospheric extension.  
662 Earth and Planetary Science Letters 234, 401–419.

663 Freeman, B., Boulton, P.J., Yielding, G., Menpes, S., 2010. Using empirical geological  
664 rules to reduce structural uncertainty in seismic interpretation of faults. Journal of  
665 Structural Geology 32, 1668-1676.

666 Gawthorpe, R.L., Jackson, C.A.-L., Young, M.J., Sharp, I.R., Moustafa, A.R., Leppard,  
667 C.W., 2003. Normal fault growth, displacement localisation and the evolution of  
668 normal fault populations: the Hammam Faraun fault block, Suez rift, Egypt. Journal  
669 of Structural Geology 25, 883-895.

670 Kim, Y-S., Peacock, D.C., Sanderson, D.J., 2003. Mesoscale strike-slip faults and  
671 damage zones at Marsalforn, Gozo Island, Malta. Journal of Structural Geology  
672 25, 793–812.

673 Lamarche, G., Barnes, P.M., Bull, J.M., 2006. Faulting and extension rate over the last  
674 20,000 years in the offshore Whakatane Graben, New Zealand continental shelf.  
675 Tectonics 25, 1–24.

676 Lamarche, G., Bull, J., Barnes, P., 2000. Constraining fault growth rates and fault  
677 evolution in New Zealand. Eos, Transactions, AGU 81, 481–496.

678 Long, J.J., Imber, J., 2011. Geological controls on fault relay zone scaling. Journal of  
679 Structural Geology 33, 1790–1800.

680 Marret, R., Allmendinger, R.W., 1991. Estimates of strain due to brittle faulting:  
681 sampling of fault populations. Journal of Structural Geology 13. 735-738.

682 Marrett, R., Allmendinger, R.W., 1992. Amount of extension on "small" faults: An  
683 example from the Viking graben. Geology 20, 47-50.

684 Mansfield, C.S., Cartwright, J. A., 1996. High resolution fault displacement mapping  
685 from three-dimensional seismic data: evidence for dip linkage during fault growth.  
686 *Journal of Structural Geology* 18, 249–263.

687 Meyer, V., Nicol, A., Childs, C., Walsh, J.J., Watterson, J., 2002. Progressive  
688 localisation of strain during the evolution of a normal fault population. *Journal of*  
689 *Structural Geology* 24, 1215–1231.

690 Moriya, S., Childs, C., Manzocchi, T., Walsh, J.J., 2005. Analysis of the relationships  
691 between strain, polarity and population slope for normal fault systems. *Journal of*  
692 *Structural Geology* 27, 1113-1127.

693 Mouslopoulou, V., Walsh, J.J., Nicol, A., 2009. Fault displacement rates on a range of  
694 timescales. *Earth and Planetary Science Letters* 278, 186–197.

695 Nairn, I., Beanland, S., 1989. Geological setting of the 1987 Edgecumbe earthquake,  
696 New Zealand. *New Zealand Journal of Geology and Geophysics* 32, 1–13.

697 Nicol, A., Walsh, J.J., Watterson, J., Underhill, J.R., 1997. Displacement rates of  
698 normal faults. *Nature* 390, 157-159.

699 Nicol, A., Walsh, J.J., Villamor, P., Seebeck, H., Berryman, K.R., 2010. Normal fault  
700 interactions, paleoearthquakes and growth in an active rift. *Journal of Structural*  
701 *Geology* 32, 1101–1113.

702 Nixon, C.W., Sanderson, D.J., Bull, J.M., 2011. Deformation within a strike-slip fault  
703 network at Westward Ho!, Devon U.K.: Domino vs conjugate faulting. *Journal of*  
704 *Structural Geology* 33, 833–843.

705 Nixon, C.W., Sanderson, D.J., Bull, J.M., 2012. Analysis of a strike-slip fault network  
706 using high resolution multibeam bathymetry, offshore NW Devon U.K.  
707 *Tectonophysics* 541-543, 69–80.

708 Peacock, D.C.P., 2002. Propagation, interaction and linkage in normal fault systems.  
709 *Earth-Science Reviews* 58, 121–142.

710 Peacock, D.C.P., Sanderson, D.J., 1993. Estimating strain from fault slip using a line  
711 sample. *Journal of Structural Geology* 15, 1513–1516.

712 Pickering, G., Bull, J.M., Sanderson, D.J., 1996. Scaling of fault displacements and  
713 implications for the estimation of sub-seismic strain. Geological Society, London,  
714 Special Publication 99, 11-26.

715 Putz-Perrier, M.W., Sanderson, D.J., 2008a. The distribution of faults and fractures and  
716 their importance in accommodating extensional strain at Kimmeridge Bay, Dorset,  
717 UK. Geological Society, London, Special Publications 299, 97-111.

718 Putz-Perrier, M.W., Sanderson, D.J., 2008b. Spatial distribution of brittle strain in  
719 layered sequences. *Journal of Structural Geology* 30, 50-64.

720 Putz-Perrier, M.W., Sanderson, D.J., 2010. Distribution of faults and extensional strain  
721 in fractured carbonates of the North Malta Graben. *AAPG Bulletin* 94, 435-456.

722 Soliva, R., Schultz, R. A., 2008. Distributed and localized faulting in extensional  
723 settings: Insight from the North Ethiopian Rift–Afar transition area. *Tectonics* 27,  
724 TC2003.

725 Taylor, S.K., 2003. A long timescale high-resolution fault activity history of the  
726 Whakatane Graben, New Zealand. PhD Thesis, University of Southampton, UK.

727 Taylor, S.K., Bull, J.M., Lamarche, G., Barnes, P.M., 2004. Normal fault growth and  
728 linkage in the Whakatane Graben, New Zealand, during the last 1.3 Myr. *Journal*  
729 *of Geophysical Research* 109, B02408.

730 Walsh, J.J., Watterson, J., Yielding, G., 1991. The importance of small scale faulting in  
731 regional extension. *Nature* 351, 391-393.

732 Walsh, J.J., Watterson, J., 1992. Populations of faults and fault displacements and their  
733 effects on estimates of fault-related regional extension. *Journal of Structural*  
734 *Geology* 14, 701-712.

735 Walsh, J.J., Childs, C., Imber, J., Manzocchi, T., Watterson, J., Nell, P. A. R., 2003.  
736 Strain localisation and population changes during fault system growth within the  
737 Inner Moray Firth, Northern North Sea. *Journal of Structural Geology* 25, 307–315.

738 Wright, I., 1990. Late Quaternary faulting of the offshore Whakatane Graben, Taupo  
739 Volcanic Zone, New Zealand. *New Zealand Journal of Geology and Geophysics*  
740 33, 245–256.

741

742

**Table 1. The estimated ages of horizons H1- H4, from Bull et al. (2006).**

<b>Horizon</b>	<b>Age</b>
H1	9+/-1 ka
H2	11.4+/-1 ka
H3	13.9+/-1 ka
H4	17+/-1 ka

**Table 2. Displacement rates for different time intervals over the last 17 kyr calculated from the throws of faults at each horizon. The proportions contributed by the Rangitaiki Fault and HW and FW faults are also indicated.**

<b>Time Interval</b>	<b>Average Displacement Rate (mm/yr)</b>				
	<i><b>Total</b></i>	<i><b>Rangitaiki Fault</b></i>		<i><b>HW and FW faults</b></i>	
17 ka - Present	6.7	2.8	42.6%	3.8	57.4%
17 - 13.9 ka	11.1	4.0	36.0%	7.1	64.0%
13.9 - 11.4 ka	4.9	1.8	37.5%	3.0	62.5%
11.4 - 9 ka	6.9	2.8	41.3%	4.0	58.7%
9 ka - Present	5.6	2.7	48.4%	2.9	51.6%

**Table 3. 3-D strain values of the fault network at H4. Comparing the strain distribution within the area of localized faulting and the area of distributed faulting.**

	Localized Area		Distributed Area		Entire Area	
	% Extension	Plunge/ Azimuth	% Extension	Plunge/ Azimuth	% Extension	Plunge/ Azimuth
<b>Overall</b>	0.83	15/315	0.85	12/327	0.83	13/324
<b>Rangitaiki Fault</b>	0.72	15/311	0.30	14/321	0.47	15/315
<b>HW and FW faults</b>	0.13	14/337	0.56	11/331	0.38	11/332
<b>RF:HW/FW</b>	<b>85%:15%</b>		<b>35%:65%</b>		<b>55%:45%</b>	

**Table 4. Heterogeneity measures for the distribution of faulting ( $V_f$ ) and extensional strain ( $V_s$ ) of each Boomer line.  $D^+$  and  $D^-$  are the maximum deviations above and below the cumulative uniform distribution, respectively.**

Boomer	Strike Distance	Fault Frequency			Extensional Strain		
		$D^+$	$D^-$	$V_f$	$D^+$	$D^-$	$V_s$
171	0	0.43	-0.02	0.45	0.68	-0.19	0.87
170	200	0.43	0.00	0.43	0.68	-0.13	0.81
169	400	0.44	-0.05	0.49	0.63	-0.15	0.78
168	600	0.46	-0.02	0.47	0.58	-0.13	0.71
104	1100	0.48	-0.08	0.56	0.52	-0.14	0.66
108	1493	0.53	-0.09	0.61	0.56	-0.14	0.70
112	1900	0.58	0.00	0.58	0.59	-0.14	0.72
114	2100	0.58	0.00	0.58	0.58	-0.21	0.79
116	2300	0.59	0.00	0.59	0.59	-0.21	0.79
117	2404	0.59	0.00	0.59	0.59	-0.26	0.84
120	2700	0.39	-0.01	0.40	0.53	-0.21	0.74
121	2800	0.39	0.00	0.39	0.52	-0.19	0.71
122	2907	0.32	0.00	0.32	0.42	-0.15	0.57
124	3105	0.34	0.00	0.34	0.38	-0.11	0.49
125	3197	0.35	0.00	0.35	0.36	-0.10	0.45
126	3300	0.22	-0.01	0.23	0.29	-0.15	0.43
128	3497	0.18	-0.16	0.34	0.18	-0.19	0.37
129	3602	0.18	-0.09	0.27	0.18	-0.23	0.42
130	3697	0.23	0.00	0.23	0.22	-0.17	0.38
132	3894	0.20	-0.02	0.22	0.16	-0.17	0.33
133	4000	0.22	-0.02	0.23	0.15	-0.15	0.30
134	4100	0.19	-0.02	0.21	0.16	-0.19	0.35
136	4291	0.18	-0.01	0.19	0.16	-0.20	0.36
137	4400	0.15	-0.05	0.20	0.20	-0.20	0.41
138	4497	0.15	-0.06	0.20	0.09	-0.21	0.30
140	4700	0.17	-0.04	0.21	0.11	-0.18	0.29
142	4900	0.19	-0.05	0.24	0.12	-0.21	0.33
144	5100	0.19	-0.14	0.34	0.15	-0.21	0.35
145	5200	0.19	-0.15	0.35	0.15	-0.19	0.34
146	5300	0.19	-0.04	0.23	0.16	-0.14	0.30
148	5505	0.21	-0.04	0.25	0.20	-0.15	0.35
150	5700	0.22	-0.04	0.26	0.24	-0.15	0.39
154	6106	0.27	-0.08	0.34	0.27	-0.24	0.51
158	6498	0.27	-0.07	0.34	0.28	-0.26	0.54



Figure 1. Location map of the Whakatane Graben within the Bay of Plenty, New Zealand showing the position of the Rangitaiki Fault and the study area, modified from Lamarche et al. (2006). The position of the high resolution seismic reflection survey lines are also shown.

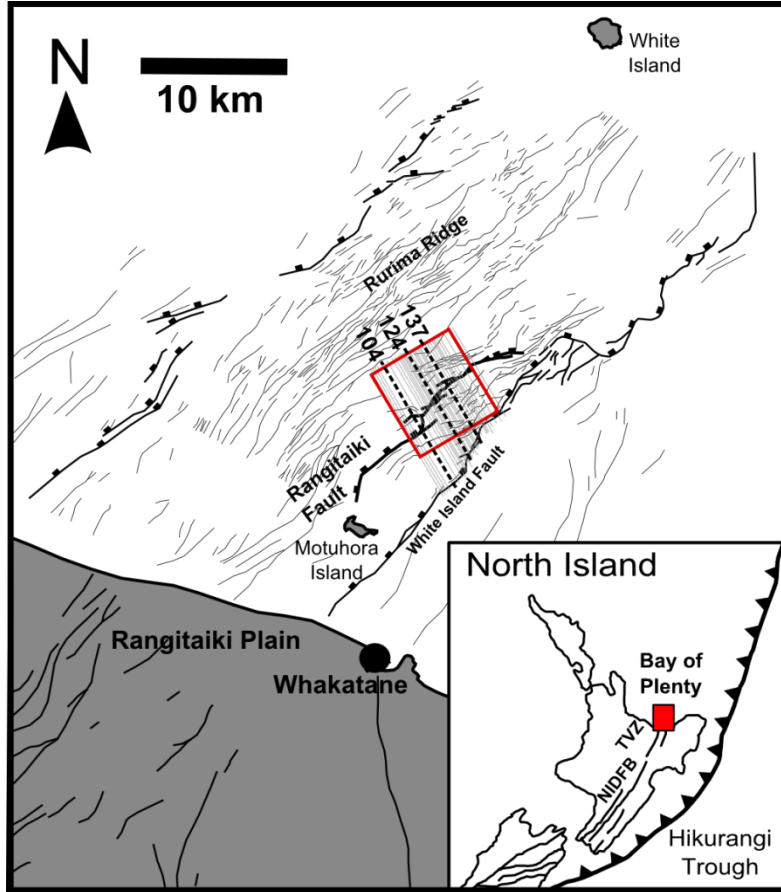


Figure 2. a) Map of the entire Rangitaiki Fault at multichannel seismic horizon MCS1 ( $300 \pm 100$  ka), modified from Bull et al. (2006). The segments of the Rangitaiki Fault are numbered, the thickness of the fault represents the displacement as it varies along strike, and dots show fault tips. Other faults are in thinner solid lines. Bathymetric contours are shown. The position of the Figure 3 is indicated as is the profiles shown in b and c (dashed line). b) The Rangitaiki fault imaged by multichannel seismic data shows that it is an extensional growth fault offsetting horizons MCS1-3 with no measurable displacement on the MCS data at the seabed. The fault offsets three clear horizons and the fault dip ranges from  $59 - 63^\circ$  over this depth interval (Taylor et al., 2004). c) Example boomer profile illustrating the Rangitaiki fault. H4 is the post-glacial transgressive surface. Fault dip in the near-surface sediments is in the range  $70 - 80^\circ$ .

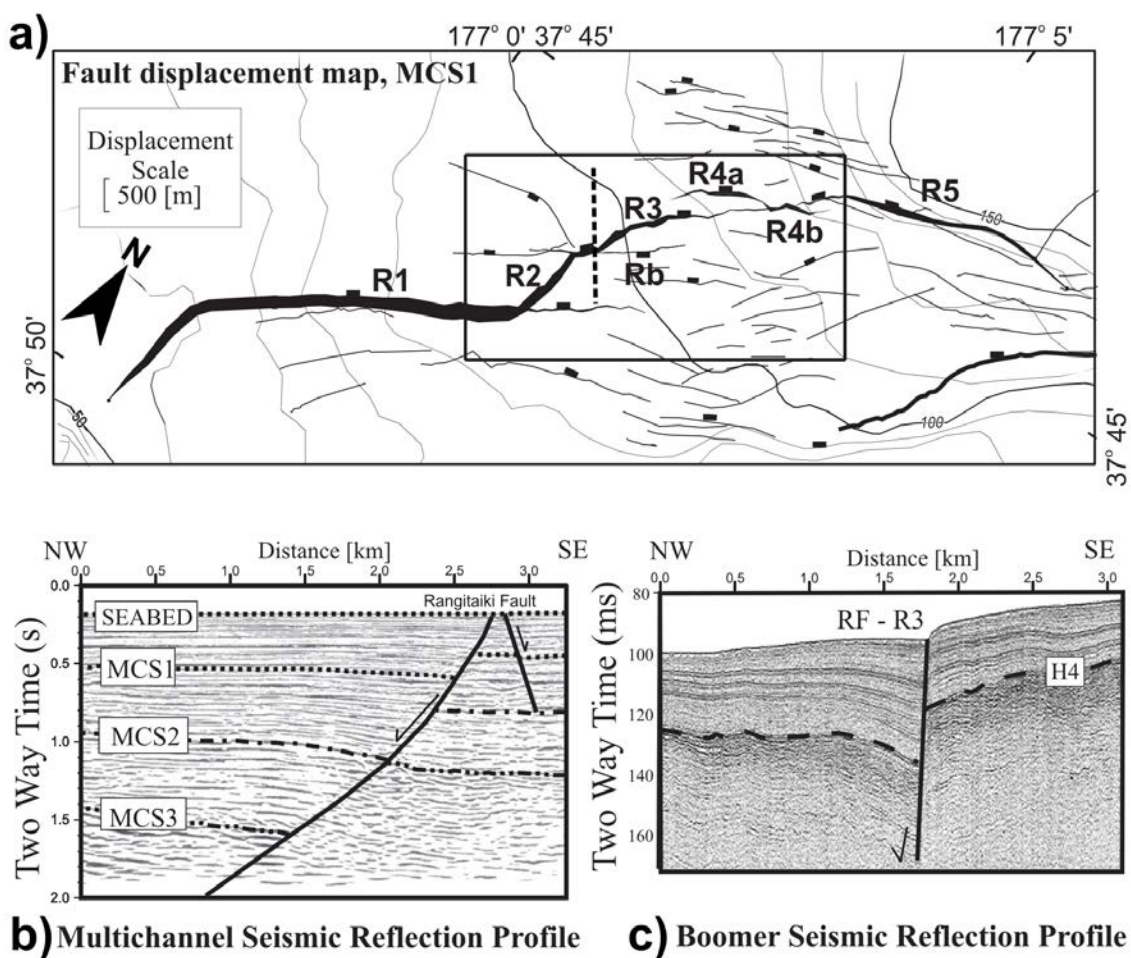


Figure 3. Spatial and displacement rate evolution for the Rangitaiki Fault system, within the location box in Figure 2, in map view, for four time periods. This uses displacement rate data from Taylor (2003) and Taylor et al. (2004) from multichannel seismic data and high resolution boomer data illustrated in figure 2. The thickness of the fault is proportional to its displacement rate during the time interval. Note that segment R1 continues south of the area (see Figure 2). These maps show the progression from isolated faults (a) to a fully linked fault system (d), and illustrate the changing fault growth mechanisms from tip propagation (i.e. R3, figures 3a to c) to linkage (i.e. R2; figures 3c and d). South-west of location 1 (d) segments R1-3 are geometrically ( $G_L$ ) and kinematically linked ( $K_L$ ), whereas north-east of location 1 (d) segments R3-R5 are geometrically linked and only partially linked kinematically ( $K_P$ ).

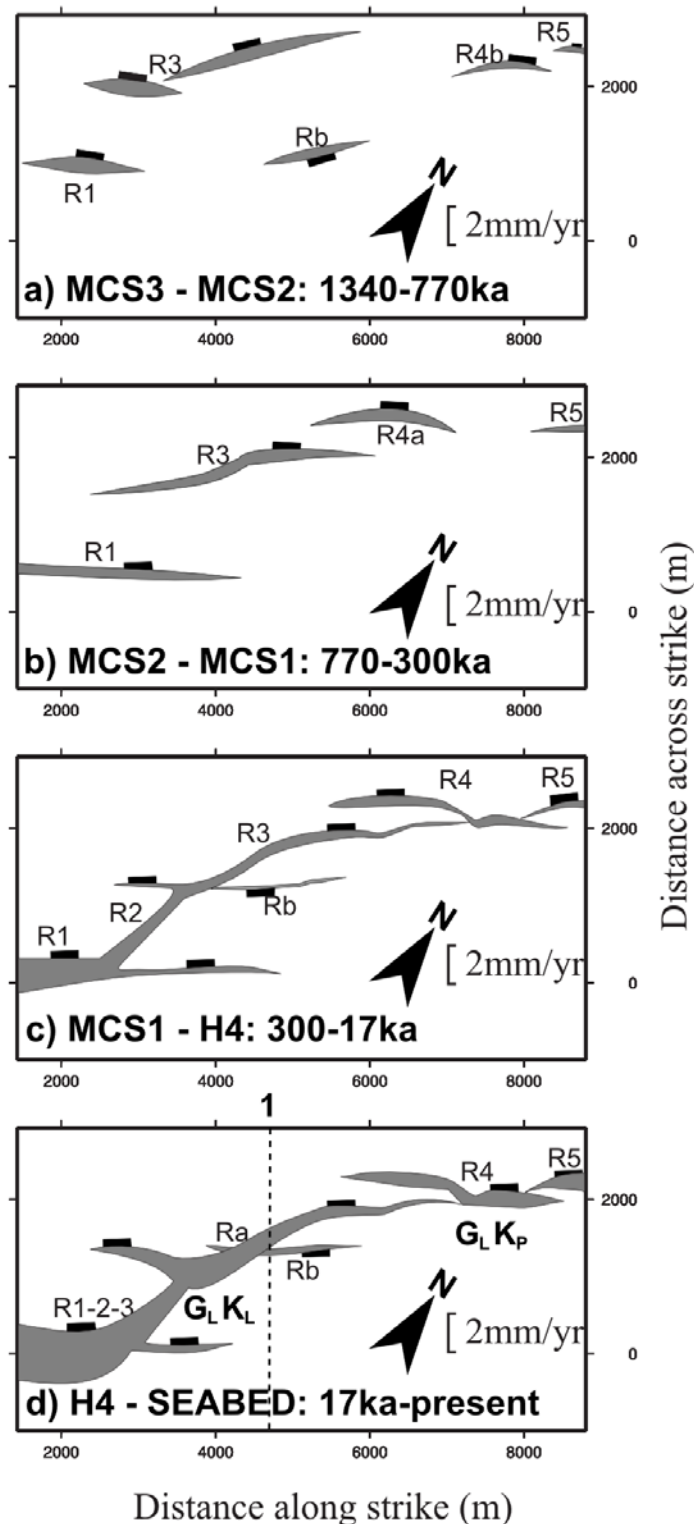


Figure 4. Interpreted seismic reflection profiles for boomer lines 104, 124 and 137 (positions shown in Figure 6) with horizons H1-H4 indicated. The fault segments which make up the Rangitaiki Fault system and the White Island Fault are also shown. Blue and red represent faults which down throw to the north and south, respectively. Note increase in fault frequency from line 104 to line 137. See supplementary material for high resolution profile example of line 124.

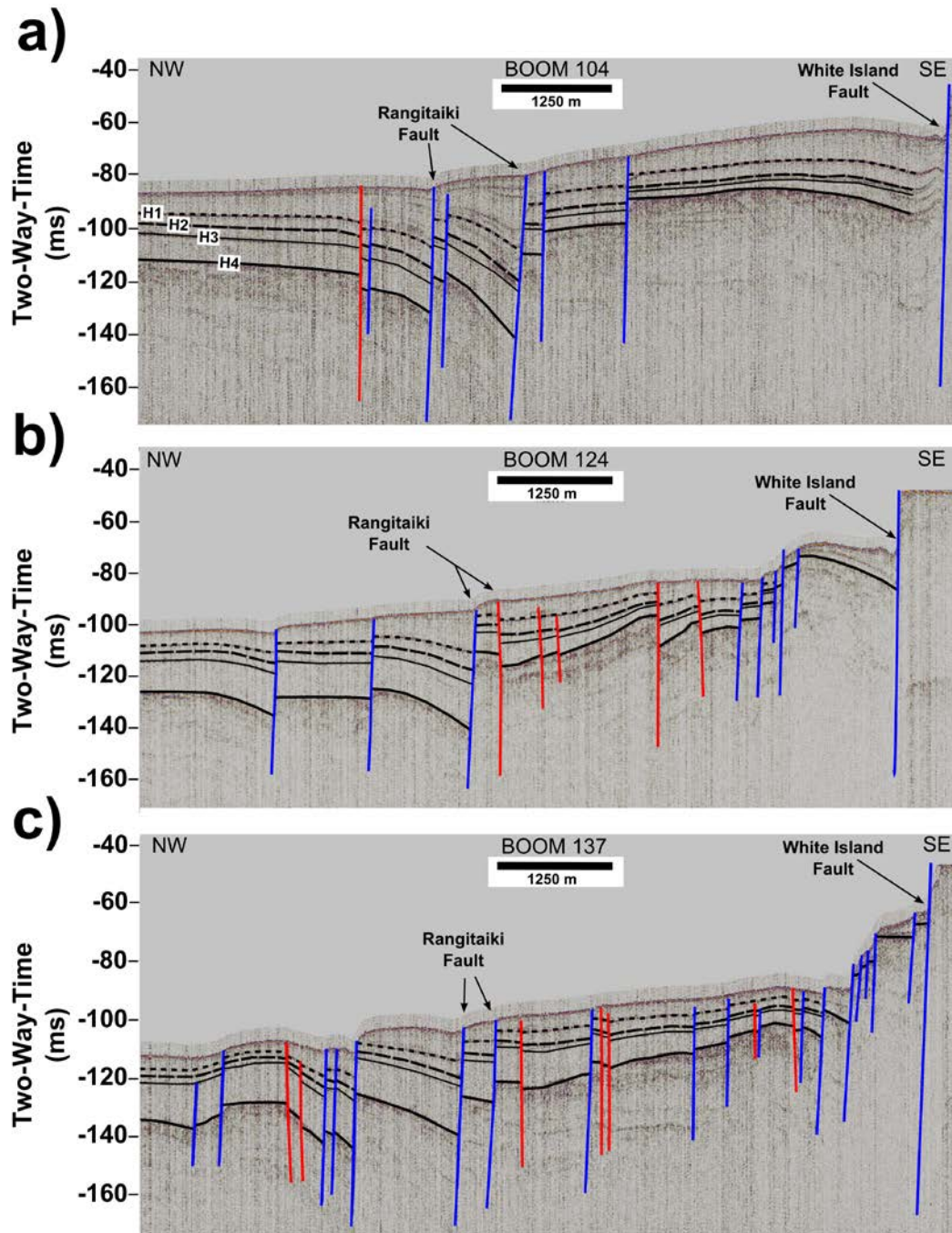


Figure 5. Schematic diagram illustrating the different geometrical and kinematic parameters of the Lagrangian strain tensor used to calculate the 3-D strain for a fault dipping  $\theta$  towards  $\Phi$ . Where  $A$  is the area of the sample plane;  $t$  is the trace-length of the fault plane;  $u$  and  $n$  are unit vectors parallel to the slip direction and perpendicular to the fault plane, respectively, that form the displacement tensor. See the text for a more detailed description.

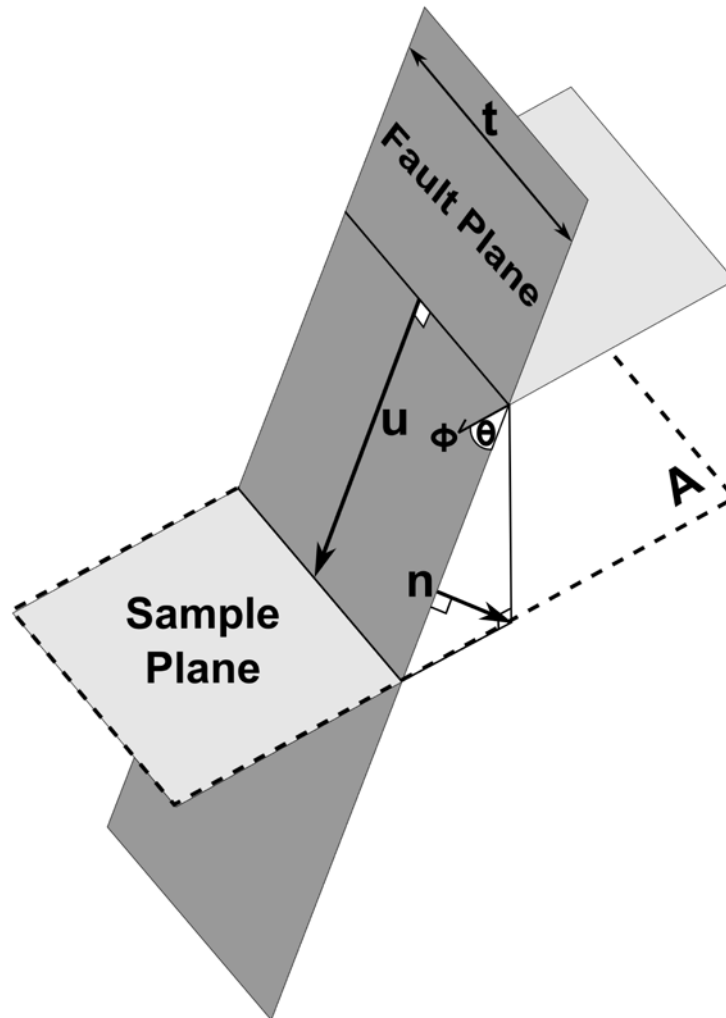


Figure 6. a) A fault map of the study area showing the segments of the Rangitaiki Fault (R1-R5; Bull et al., 2006). The hanging wall and footwall fault groups are NW and SE of the Rangitaiki Fault, respectively. The position of seismic reflection profiles illustrated in Figure 4 are also shown. b) Length-weighted rose diagrams showing the fault trends within each fault group.

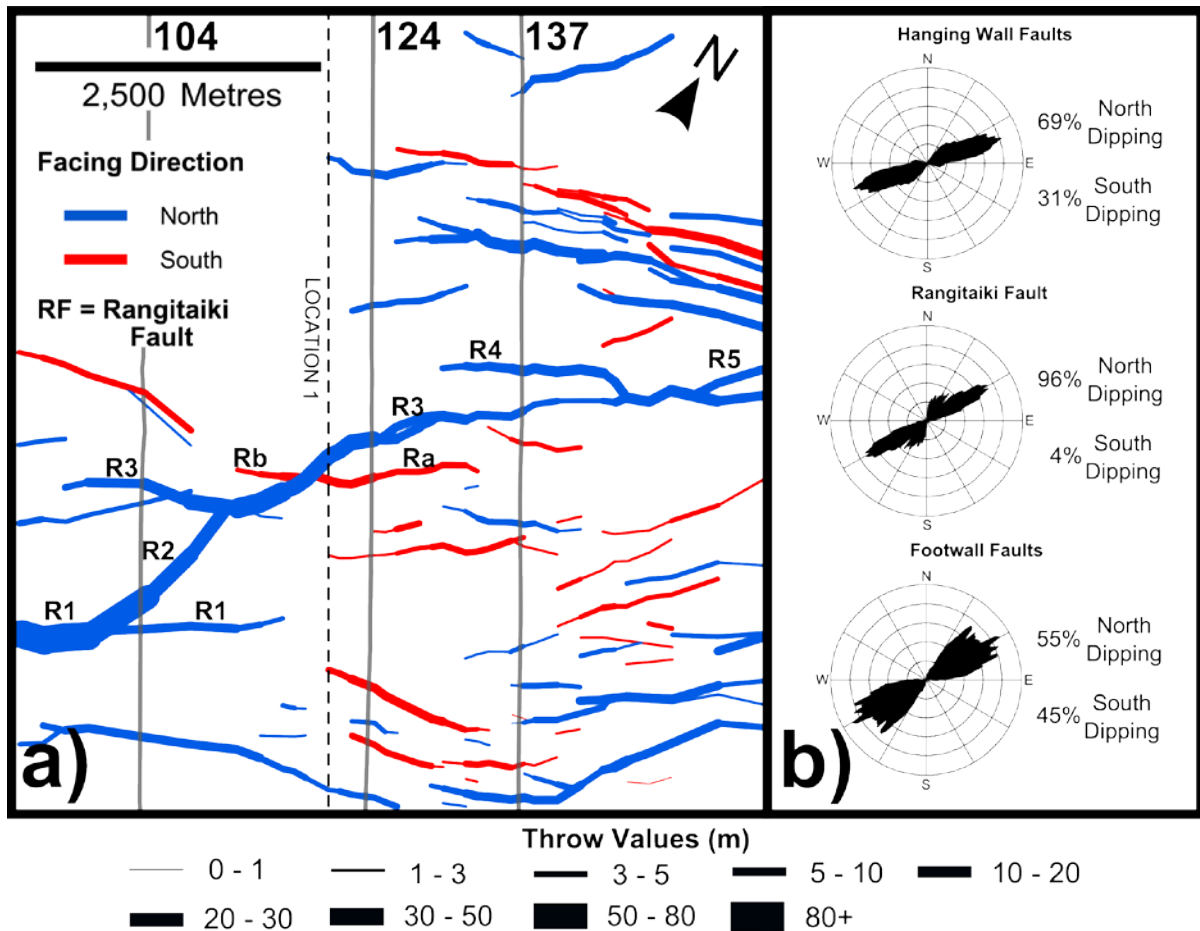


Figure 7. Profiles of cumulative displacement along strike of the fault network for horizons H1- H4 (ages 9 ka, 11.4 ka, 13.9 ka and 17 ka, respectively) of: a) the entire fault network; b) the Rangitaiki Fault and c) the Hanging wall and Footwall faults. d) A fault map weighted by displacement shows the positions of locations 1- 5.

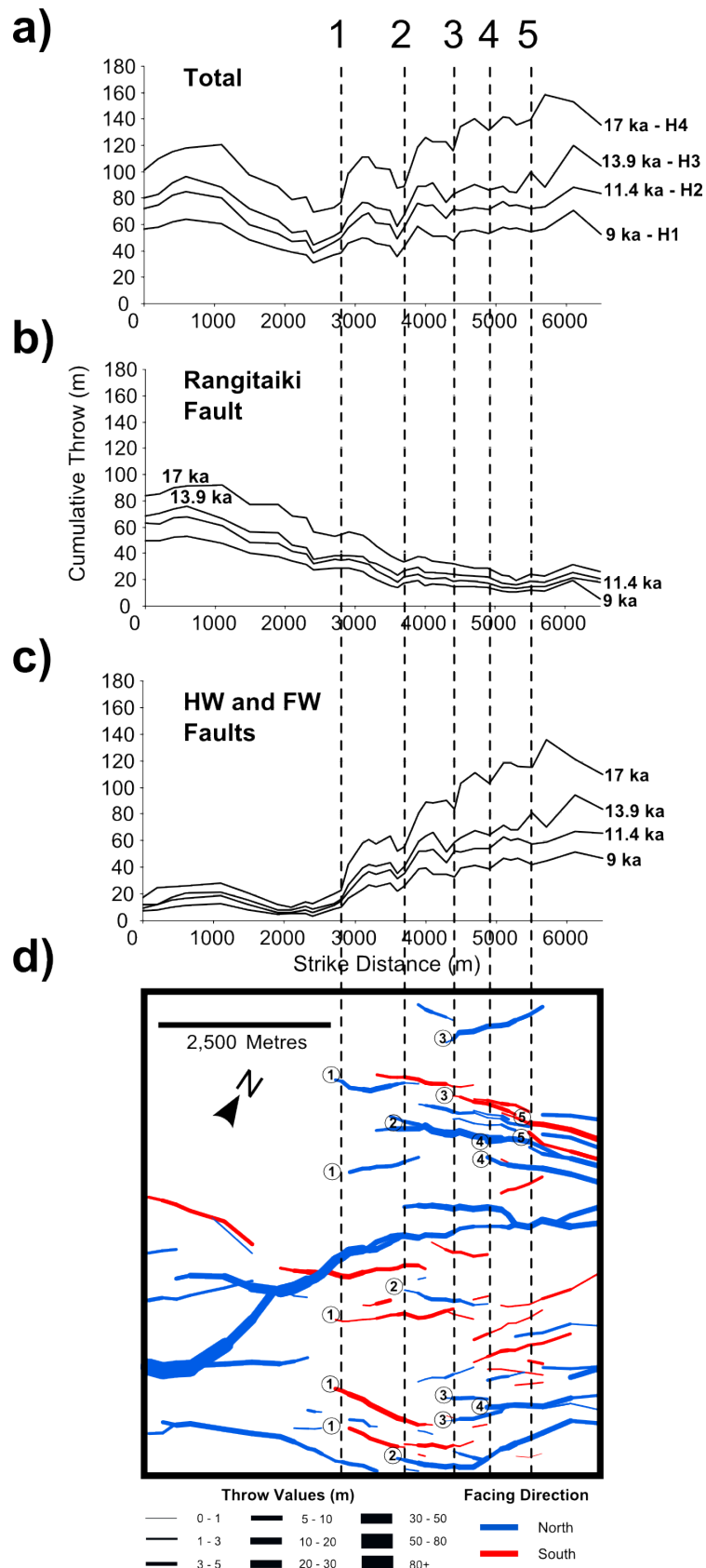
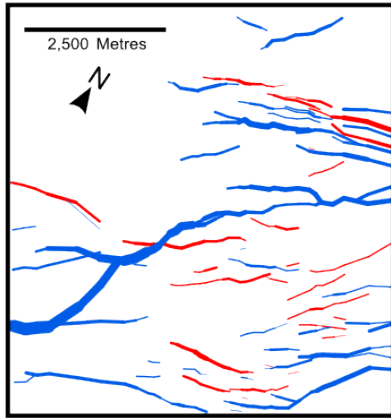
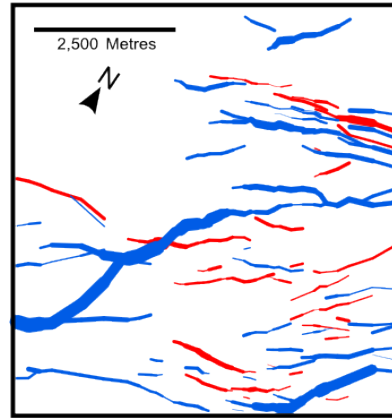


Figure 8. Fault maps showing the displacement rates of each fault within the fault network for different time intervals over the last 17 kyr: a) 17 kyr-Present; b) 17-13.9 kyr; c) 13.9-11.4 kyr; d) 11.4-9 kyr; e) 9 kyr-Present.

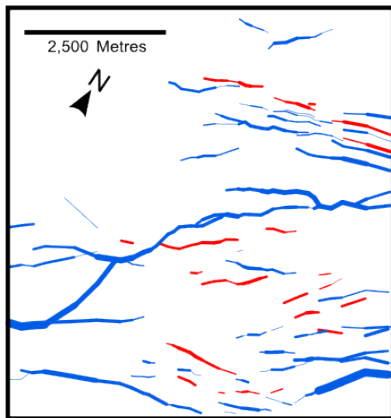
a) 17kyr - Present



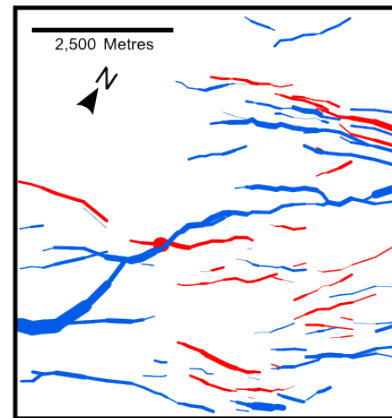
b) 17 - 13.9kyr



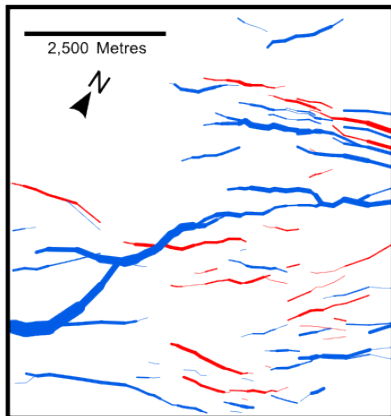
c) 13.9 - 11.4kyr



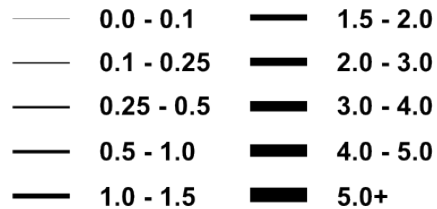
d) 11.4 - 9kyr



e) 9kyr - Present



**Throw Rates (mm/yr)**



**Facing Direction**



Figure 9. Displacement rate variations along strike of the fault network comparing the displacement rates of the Rangitaiki Fault (black) to the hanging wall and footwall faults (grey) for: a) 17 kyr-Present; b) 17-13.9 kyr; c) 13.9-11.4 kyr; d) 11.4-9 kyr; e) 9 kyr-Present. Location 1 marks the change from localized faulting to distributed faulting.

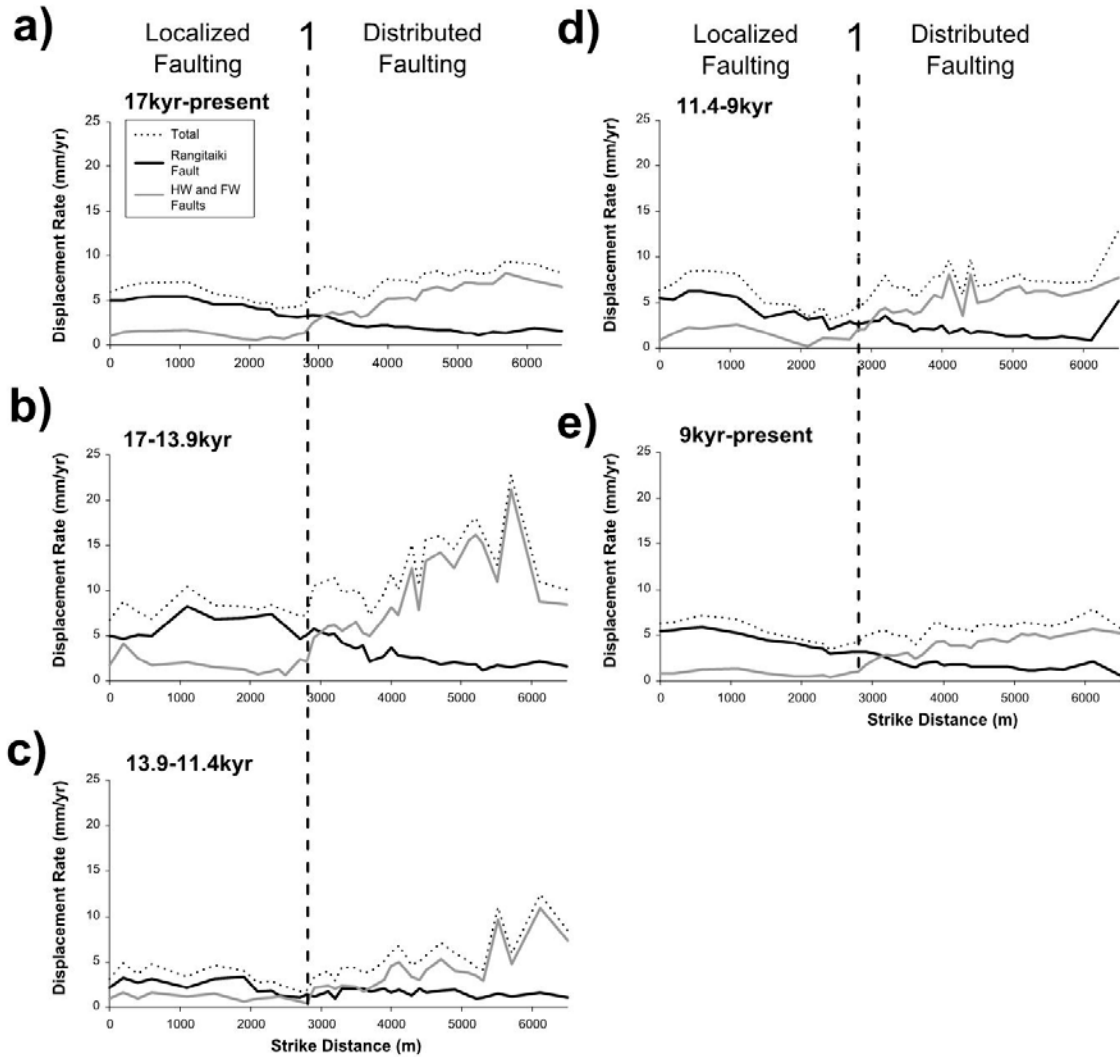


Figure 10. a) Strain profile for H4 indicating the variations in the % extension of each boomer line along strike of the fault network showing the strain accommodated by the Rangitaiki Fault (black) and the hanging wall and footwall faults (grey). b) Cumulative plot of % extension showing the contribution of each fault to the overall extension of boomer lines 104, 124 and 137 (positions are indicated in Figure 6a). These also show the contribution to strain from the different segments of the Rangitaiki Fault, which are highlighted by the grey boxes.

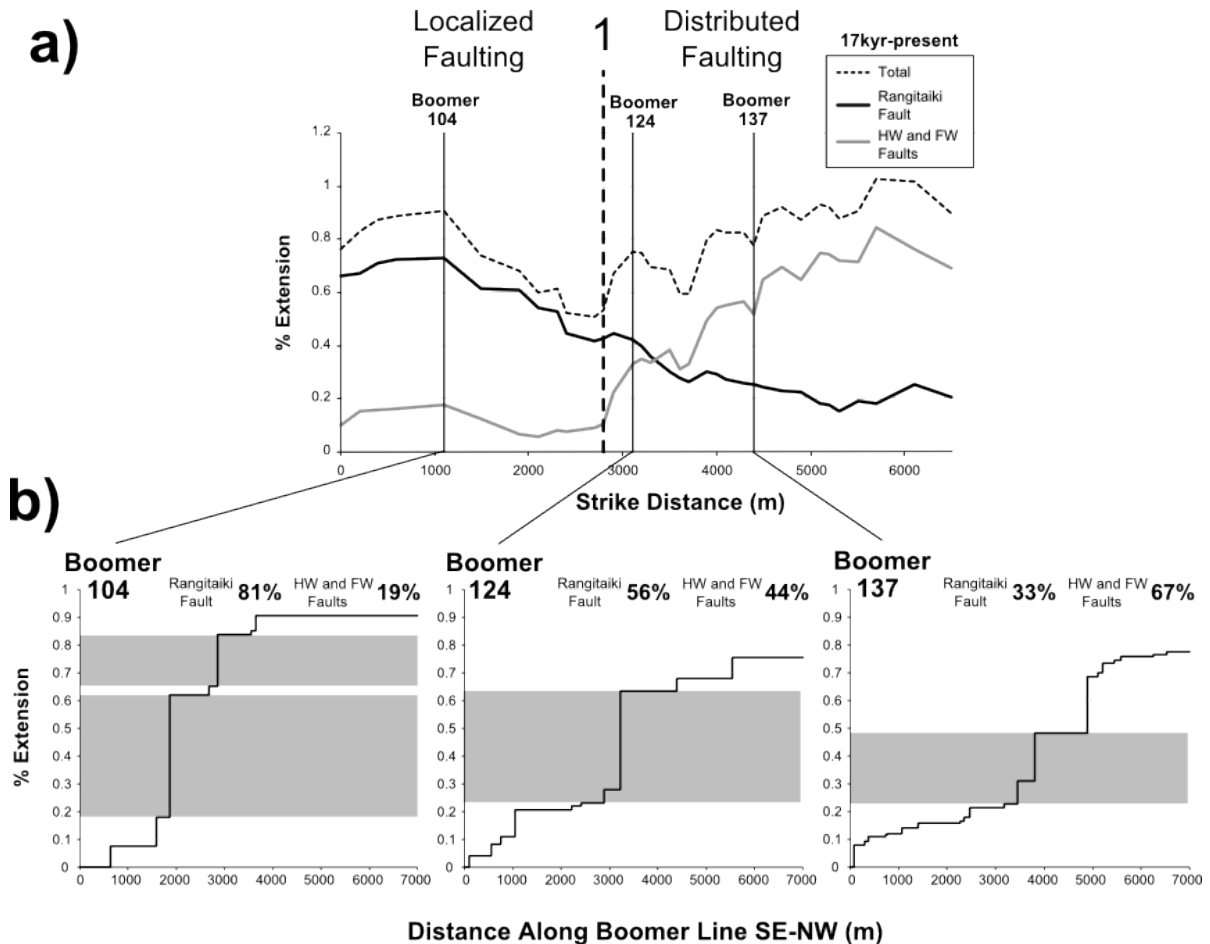


Figure 11. a), b) and c) are selected normalized cumulative plots for boomer lines 104, 124 and 137 showing the spatial distribution of fault numbers (dashed grey) and extensional strain (solid black). These are worked examples to show the maximum deviations above and below the cumulative uniform distribution and the values for  $V_f$  and  $V_s$ . d) and e) show the along strike variations of the heterogeneity measures  $V_f$  and  $V_s$ , respectively. Location 1 marks the change from localized faulting to distributed faulting.

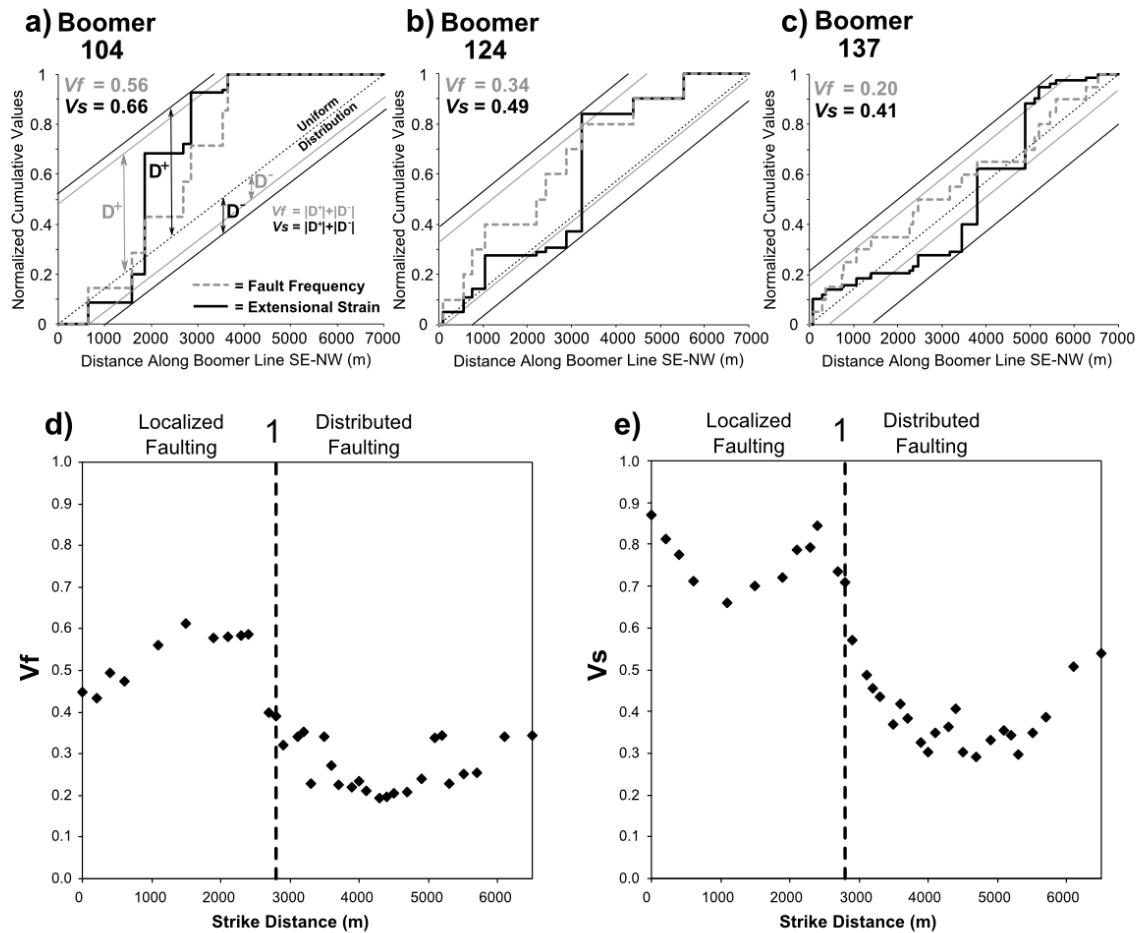
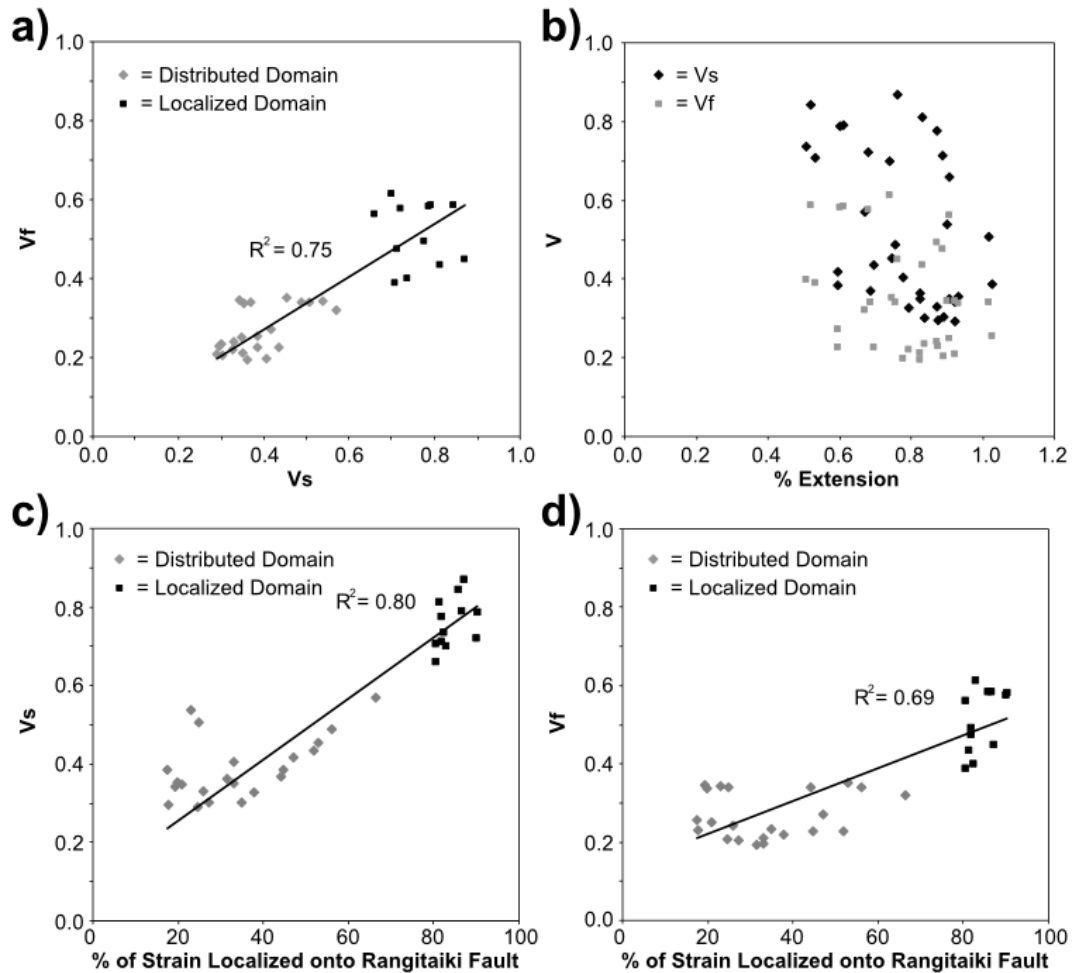


Figure 12. (a) Plot comparing the spatial heterogeneity measures of faulting  $V(f)$  and strain ( $V_s$ ) for each boomer line. (b) Heterogeneity measures compared with the overall extension accommodated by each boomer line; c) and d) indicate the relationship between the proportion of strain localized onto the Rangitaiki Fault and the spatial heterogeneity of  $V(f)$  and strain ( $V_s$ ) respectively. See text for description of heterogeneity measures.



**Figure 13. 3-D block diagrams summarizing the differing characteristics in the spatial distribution of strain and faulting for a) a localized domain of faulting versus b) a distributed domain of faulting.**

